Transdimensional inversion of ambient seismic noise for 3D shear velocity structure of the Tasmanian crust

Mallory K. Young[1], Nicholas Rawlinson[1], and Thomas Bodin[2]

ABSTRACT

Ambient seismic noise tomography has proven to be a valuable tool for imaging 3D crustal shear velocity using surface waves; however, conventional two-stage inversion schemes are severely limited in their ability to properly quantify solution uncertainty and account for inhomogeneous data coverage. In response to these challenges, we developed a two-stage hierarchical, transdimensional, Bayesian scheme for inverting surface wave dispersion information for a 3D shear velocity structure and apply it to ambient seismic noise data recorded in Tasmania, southeast Australia. The key advantages of our Bayesian approach are that the number and distribution of model parameters are implicitly controlled by the data and that the standard deviation of the data noise is treated as an unknown in the inversion. Furthermore, the use of Bayesian inference — which combines prior model information and observed data to quantify the a posteriori probability distribution — means that model uncertainty information can be correctly propagated from the dispersion curves to the phase velocity maps and finally onward to the 1D shear models that are combined to form a composite 3D image. We successfully applied the new method to ambient noise dispersion data (1–12-s period) from Tasmania. The results revealed an east-dipping anomalously low shear velocity zone that extends to at least a 15-km depth and can be related to the accretion of oceanic crust onto the eastern margin of Proterozoic Tasmania during the mid-Paleozoic.

INTRODUCTION

Various methods for retrieving crustal shear wave velocity structure from passive seismic data have been developed over the past half-century. These include receiver function analysis (Langston, 1979; Clitheroe et al., 2001; Xu et al., 2007), surface wave dispersion measurement (Dorman and Ewing, 1962; Villaseñor et al., 2001; Mitra et al., 2011), and local earthquake tomography (Walck and Clayton, 1987; Kissling, 1988; Thurber, 1992; Eberhart-Phillips and Reyners, 1999; Wang et al., 2003; Yolsal-Çevikbilen et al., 2012). Each has its own limitations, with common shortcomings including a lack of near-surface resolution, ad hoc model parameterization, weak uncertainty estimates, dependence on an irregular distribution of earthquake sources, biases from structures outside the model region, earthquake location errors, and bandwidth limitations. The introduction of ambient seismic noise analysis (Shapiro et al., 2005; Lin et al., 2007; Yang et al., 2007; Bensen et al., 2009; Behr et al., 2010) has resolved some of these issues, because earthquakes are no longer a required component. With spatial resolution dictated largely by array geometry and the frequency content of the ambient noise, densely spaced arrays have the potential to image fine scale structures in the crust (Young et al., 2011), albeit at the expense of decreased depth penetration, which becomes shallow as interstation distance decreases. Other issues, such as the choice of model parameterization and noise level estimation, remain regardless of the data set. Uncertainty information obtained from ambient noise analysis is difficult to obtain, and thus error assessment is far from a standardized procedure (Shapiro and Ritzwoller, 2002; Bensen et al., 2009; Yao and Van der Hilst, 2009; Weaver et al., 2011). New methods that allow the data to play a more dominant role in the reconstruction process will be invaluable in tackling these limitations.

The hierarchical Bayes procedure (Box and Tiao, 1973; Bernando and Smith, 1994) is a robust technique that is insensitive to variations in parameter settings such as the allowed number of cells, total number of iterations, or the initial model. Model parameters, including the level of data noise, are represented by a probability distribution function that depends on known prior information and information provided by the data. Explicit regularization of these

model parameters is not required, thereby avoiding arbitrary decisions about the number of model unknowns or the quantification of data error. The hierarchical nature of the method means that the noise in the data is left as an unknown, making the required complexity of the solution inferred from the data themselves (Bodin et al., 2012a). Moreover, uncertainty estimates obtained from each stage of our inversion procedure are preserved and used in the following step, eliminating the need for the imprecise or ad hoc proxies for error used in more traditional, linear tomographic inversions, such as jackknife tests, posterior covariance (Rawlinson et al., 2010a), signal-to-noise ratios (Bensen et al., 2007), etc. Bayesian analysis has been applied to a variety of seismological problems, including tomography (Zollo et al., 2002; Bodin and Sambridge, 2009; Khan et al., 2011; Bodin et al., 2012a), receiver function inversion (Piana Agostinetti and Malinverno, 2010; Bodin et al., 2012b), and seismic source parameter estimation (Arnold and Townend, 2007; Myers et al., 2007; Monelli and Mai, 2008; Walsh et al., 2009).

Conventional approaches to obtaining a 3D shear velocity model from ambient seismic noise data follow a basic procedure similar to our own (Yang et al., 2008a, 2008b; Yao et al., 2008; Bensen et al., 2009; Stehly et al., 2009; Behr et al., 2011). First, group or phase velocity maps are produced from dispersion curves extracted from the crosscorrelation of ambient seismic noise. Generally, this is a linearized procedure that seeks to minimize some cost function and involves a subjective application of smoothing and damping, during which valuable information can be lost. We choose instead to use a fully nonlinear, Bayesian technique that produces a final model from the average of a large ensemble of models, thus avoiding the need for arbitrary smoothing or damping. The model space is partitioned by nonoverlapping, Voronoi polygons of variable number, shape, and velocity, in which the uneven spatial distribution of data is managed by relative cell size. Second, the 2D maps are sampled over a range of periods at regular intervals in latitude and longitude to produce a collection of dispersion curves. The spatial variation of uncertainty in the 2D maps is traditionally difficult to determine, and in cases in which the dispersion curves are assigned uncertainty estimates, they are often obtained via ad hoc means, such as assessing results from the application of a range of regularization parameters (Bensen et al., 2009) or introducing an arbitrary proportionality constant to relate uncertainty to velocity (Yao et al., 2008).

Our approach provides an inherent estimate of model uncertainty through the assessment of the standard deviation of the ensemble of 2D models at each grid point. Each curve is then inverted for a 1D shear velocity model. Even methods that use other nonlinear inversion techniques, such as nontransdimensional Markov chain Monte Carlo (MCMC) sampling or the neighborhood algorithm (NA) (Sambridge, 1999), are limited in that they use dispersion data without accurate uncertainty estimates (Yang et al., 2008a; Yao et al., 2008; Bensen et al., 2009; Stehly et al., 2009; Behr et al., 2010). Furthermore, model space is often not fully explored, and there is moderate dependence of the final model on the initial model. On the other hand, a Bayesian inversion allows a more complete sampling of model space and produces results that are independent of the initial, random model. Conventional methods also require arbitrary decisions about model parameterization. The number of crustal layers is generally limited to three, and layer thickness is either fixed or limited in its ability to vary (Yang et al., 2008a,

2008b; Yao et al., 2008; Bensen et al., 2009; Stehly et al., 2009). Moreover, the determination of the final, "preferred" model is often subjective in that a mean curve is produced from a selection of "best" models based on arbitrary acceptance criteria (Yang et al., 2008a, 2008b; Bensen et al., 2009; Stehly et al., 2009). We instead produce expected models from the averaging of the complete ensemble of independent and uniquely parameterized models representing the posterior probability distribution functions of velocity at each depth. Finally, the 1D models are combined to produce a pseudo-3D shear velocity model of the region. The relative superiority of our method lies in the inversion approach and uncertainty analysis.

In this study, we show that our Bayesian inversion technique can be successfully applied to ambient seismic noise data to yield a 3D shear velocity model complete with uncertainty estimates. Our target region is the southeast Australian island of Tasmania, where strong ambient noise signals are generated by the surrounding ocean. Due to several factors, including widespread cover of Jurassic dolerites and younger sediments, which mask vast tracts of underlying basement, many aspects of Tasmanian tectonics remain contentious. Most notably, there exist many theories for the evolution of the Tasmanian lithosphere during the Paleozoic era, and its tectonic relationship to mainland Australia remains enigmatic (Reed et al., 2002; Foster et al., 2005; Berry et al., 2008; Gibson et al., 2010; Cayley, 2011). For instance, a first-order feature of Tasmanian geology is that the western part of the island (West Tasmania Terrane, or WTT) is dominated by outcrop of Proterozoic origin, whereas the eastern part of the island (East Tasmania Terrane, or ETT) has only Phanerozoic outcrop. The so-called Tamar fracture system (TFS) has traditionally been used to mark the boundary between the two terrains. This stark contrast between geologic regimes was originally attributed to a major crustal fracture system (Williams, 1989), but recent evidence increasingly points to the TFS as being a thin-skinned feature (Leaman, 1994; Rawlinson and Urvoy, 2006; Rawlinson et al., 2010b; Young et al., 2011). However, this is the first time that a high-resolution shear velocity model of the upper crust has been produced, and our results have widespread implications for the tectonic relationship between the ETT and WTT.

PHASE VELOCITY MAPS

Data

The data for this study come from two subarrays of the WOMBAT transportable seismic array project (Rawlinson et al., 2011). The 64 short-period stations (1-s corner period) of the TIGGER array were deployed in March 2002 and span northern Tasmania, whereas the 40-station SETA array (also 1-s corner period) was installed four years later immediately south of TIGGER on the central east part of the island (Figure 1). We use approximately seven months of data from each array to perform ambient seismic noise tomography of the region.

The ambient noise crosscorrelation procedure we use is similar to that of Bensen et al. (2008). To produce the highest quality Green's functions, the noise recordings are divided into 40-min segments with 75% overlap (Seats et al., 2012). Vertical-component data are crosscorrelated and stacked for all simultaneously recording station pairs. Phase velocities are measured (Figure 2) using a modified version of the image transformation technique developed by Yao et al. (2006). To accurately measure phase velocities up to 1 Hz, we use a linear-dependence of the band-pass filter width on the

central period as introduced by Young et al. (2011). Each picked phase velocity curve is compared to its associated group velocity curve (Young et al., 2011) to help confirm the reliability of the curve and to minimize the possibility of cycle skipping.

Inversion method

After making the phase velocity measurements, a transdimensional, hierarchical, Bayesian tomographic inversion is performed for periods between 1 and 12 s. A brief description of the method is provided here; further details can be obtained from Bodin and Sambridge (2009) and Bodin et al. (2012a). For each period of interest, the 2D phase velocity field is described by a mosaic of Voronoi cells of variable size, position, and shape (Figure 3). The method is "transdimensional" in that the number of cells is allowed to vary throughout the course of the inversion and "hierarchical" in that it has two levels of inference. At the higher level are "hyperparameters" such as the noise variances of the data. Here, data "noise" refers to whatever our model cannot explain (Scales and Snieder, 1998; Bodin et al., 2012a), which can be attributed to measurement errors, shortcomings of the forward model, and mathematical or theoretical approximations. At the lower level are the physical parameters that represent earth properties, e.g., seismic velocities. Information on physical parameters at the lower level is conditional on the values of hyper-parameters selected at the upper level. A posterior probability distribution is defined for hyperparameters (e.g., data noise variances) and earth parameters (e.g., Voronoi cell location, Voronoi cell velocity, and total number of cells). One free parameter (hyper-parameter) is assigned to model

the noise in the traveltime measurements of the Green's functions when filtered at central periods of 1–12 s. We make the assumption that, for a given period, all phase velocity curves have the same level of uncertainty. By inverting for the data uncertainty at each period, we allow the level of complexity and strength of perturbations in the final model to be appropriately limited by the noise content of the data (e.g., Piana Agostinetti and Malinverno, 2010).

We can extract meaningful quantities from the posterior probability distributions such as the mean, median, or maximum. Based on the Bayes' theorem (Bayes, 1763), we express the posterior distribution as follows:

$$p(\mathbf{m} \mid \mathbf{d}_{obs}) \propto p(\mathbf{d}_{obs} \mid \mathbf{m})p(\mathbf{m}), \qquad (1)$$

where $p(\mathbf{m} \mid \mathbf{d}_{obs})$ is the probability distribution function of the unknown model parameter $\mathbf{m}$ given the data ($\mathbf{d}$). The term $p(\mathbf{d}_{obs} \mid \mathbf{m})$ is the likelihood function, which yields the probability of observing data (d) given model (m). The likelihood function $p(\mathbf{d}_{obs} \mid \mathbf{m})$ depends on the misfit between the observed data and the synthetic traveltimes computed for a given model and also on the estimated variance of the data noise. Our prior information about model ($\mathbf{m}$) is represented by the a priori probability distribution $p(\mathbf{m})$. In this study, we use a uniform prior distribution between a minimum and maximum value. This prior phase velocity distribution is 2.4 km/s wide and is centered on the average velocity observed for that period. These bounds are wide enough such that the final recovered model is not hampered by the upper and lower limits. We solve the forward problem with a grid-based eikonal solver (Rawlinson and Sambridge, 2004).
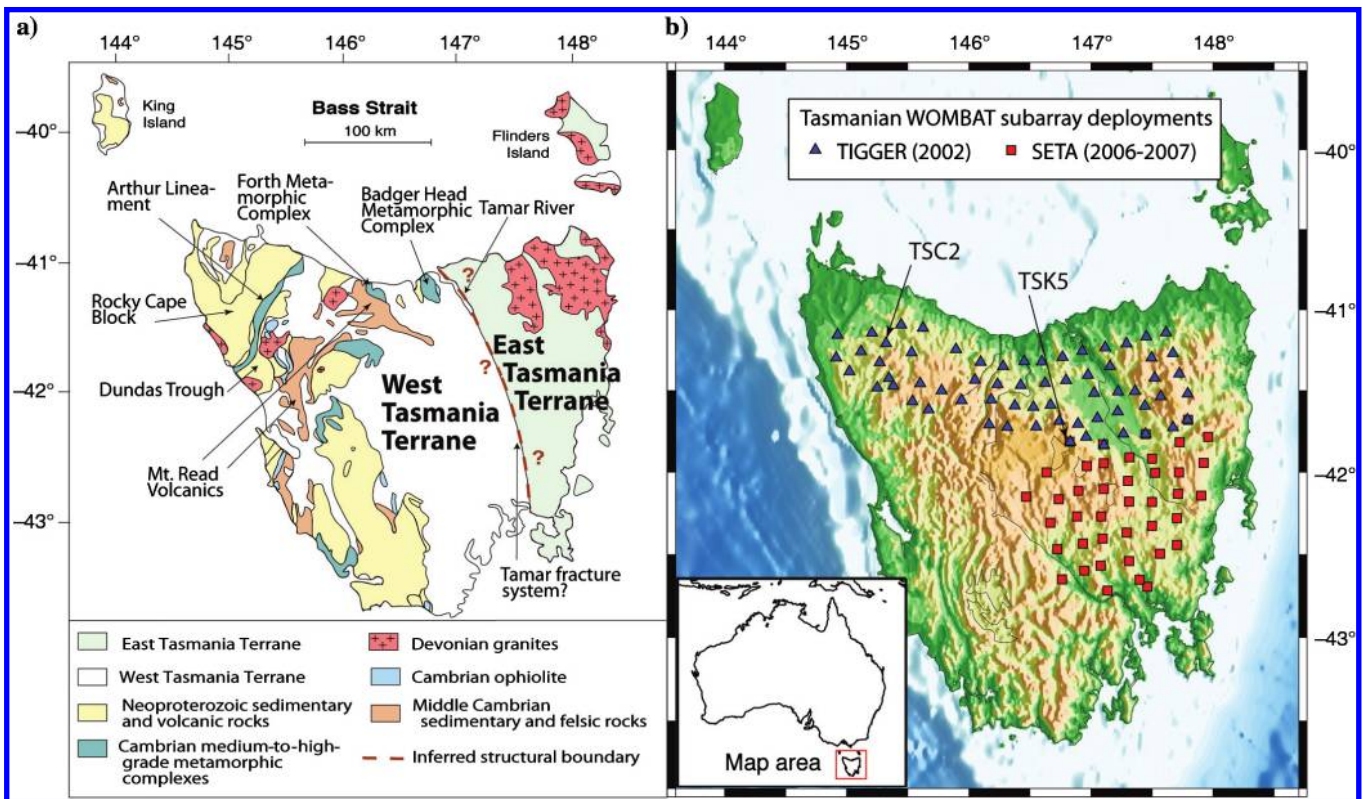

Figure 1. (a) Map of basic geologic provinces of Tasmania. Major structural features discussed in the text are identified. (b) Map of WOMBAT subarrays TIGGER and SETA used in this study.

To generate the posterior probability distribution for each model parameter, we use a generalized version of MCMC sampling called reversible jump MCMC (rj-MCMC; Green, 1995, 2003). The rj-MCMC is an iterative method of sampling the allowed parameter space. The initial model is randomly generated, and subsequent iterations in the random sequence are based on a proposal probabil-
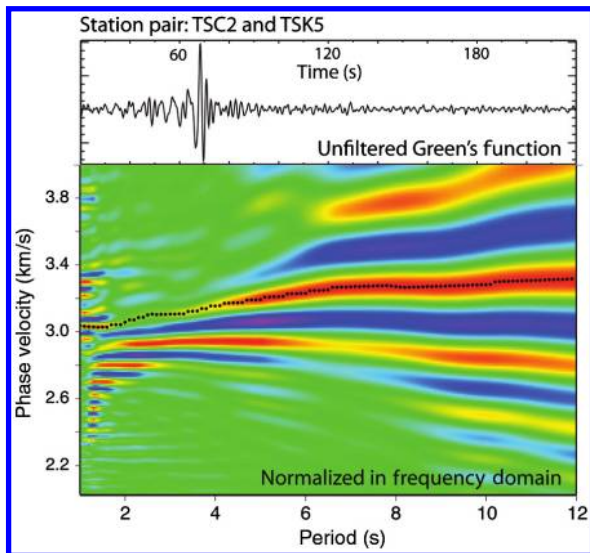

Figure 2. (top) The raw, symmetric component crosscorrelation function corresponding to the TIGGER station pair TSC2 and TSK5 (interstation distance of 143 km) (Figure 1). (bottom) Corresponding phase velocity dispersion curve that has been normalized in the frequency domain. The dotted black line represents the picked dispersion curve that is dependent on the earth structure between this pair.
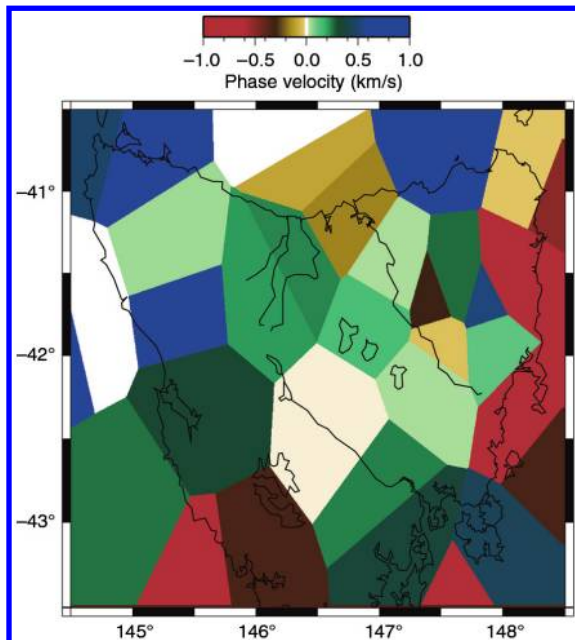

Figure 3. Example of a Voronoi cell model, which consists of an irregular, interlocking set of polygons that partition the plane. Each Voronoi cell encompasses all points of the 2D space that are closer to its center than to any other Voronoi cell center.

ity distribution (refer to Bodin et al. [2012b] for a more complete description). After a large number of "burn-in" iterations, the rj-MCMC sampler converges to a stable configuration according to the posterior distribution (Green, 1995, 2003). At each iteration, a proposed model is created from a random perturbation of the current model. This proposal is then either accepted or rejected. Proposed models that fit the data better than the original model are always accepted. Proposed models that fit the data worse than the original can also be accepted, but only a fraction of the time. This fraction depends on the ratio of the likelihood of producing the observed data with the proposed model over the likelihood of producing the observed data with the current model. The first portion of burn-in iterations is omitted from the final ensemble of models because the sampling has not yet become stable nor representative of the true posterior probability distribution. We take the average of this ensemble of models to produce our final, preferred model. Because the Voronoi cells can occupy an infinite range of configurations, taking the average of a large number (on the order of 10^5 models for 160 independently run Markov chains) of post-burn-in models creates a continuous final model. This average model contains more detail than any one individual model but none of the artificial discontinuities inherent to the base parametrization. There is no need to apply smoothing or damping procedures because the perceived model complexity and smoothness are innate to the averaged solution. Although it may seem like an overly complex model would result to maximize data variance reduction, the parsimonious nature of the Bayesian approach promotes the preservation of the simplest models that fit the data, thus preventing unjustified model complexity (Bodin et al., 2012a).

Results

Thanks to the close spacing of the TIGGER and SETA arrays (with interstation distances of approximately 15 km), we have produced phase velocity maps for periods between 1 and 12 s (Figure 4). Model parameter convergence is achieved for all periods after 50,000 iterations. Every 50th model of the subsequent 120,000 iterations is used to create the final average model. Simultaneous yet independent sampling of the model space was facilitated through the parallel use of 160 CPU cores for 4 h (640 CPU h). The standard deviation of the phase velocity at each grid node is extracted from the ensemble of phase velocity maps and provides a good estimate of the spatial variation in uncertainty for each map (Figure 4). This information is later used in the inversion for shear velocity.

Model complexity is greatest for periods between 3 and 9 s. This is due to a combination of factors. Maps for periods longer than 9 s have slightly higher noise estimates and increasingly fewer raypaths because phase dispersion measurements are only performed when the interstation spacing is at least three wavelengths (Bensen et al., 2008), and the short period stations will have more self-noise at longer periods. Maps for periods shorter than 3 s also have higher noise estimates (~1.05 s for a 1-s period versus ~0.31 s for an 8-s period). This is probably due to unresolvable near-surface effects, such as topography and shallow sediments, and unmodeled wave behavior, such as scattering and multipathing. Consequently, the most likely number of cells needed to represent the data is greatest for the intermediate periods. For a period of 7 s, approximately 90 cells are needed to best reproduce the data, whereas only 25 cells are needed for the 12-s period data.
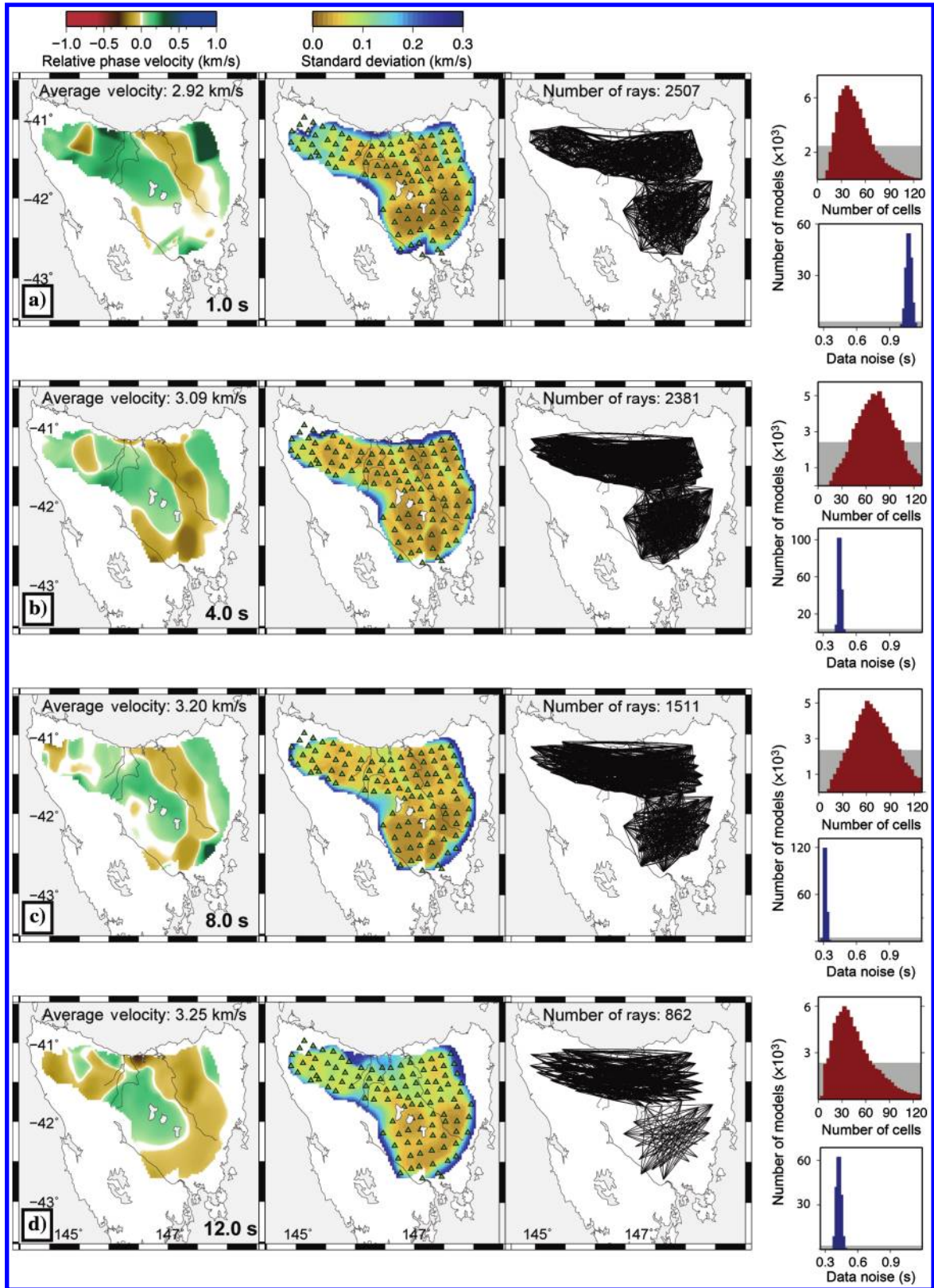
Figure 4. Phase velocity maps for periods of (a) 1.0, (b) 4.0, (c) 8.0, and (d) 12.0 s (left) are shown with their corresponding standard deviation plots and ray path coverage plots. Phase velocities are relative to the "average velocity" given in the top right of each map. Phase velocity and standard deviation maps are trimmed according to the contour line when standard deviation is equal to 0.3 km/s. Posterior probability distribution histograms for the number of cells (red columns) and data noise (blue columns) are also shown (right). The prior distributions are indicated by shaded gray rectangles.

The root mean square (rms) values of the residuals calculated from a homogeneous model of phase velocity equal to the average phase velocity at a given period are plotted along with the rms values resulting from the final average model (Figure 4, left) in Figure 5. The estimated noise in the data prevents further reduction of the rms values. Unlike traditional linear inversions that seek to produce a single model that minimizes the variance of the data, the Bayesian method produces an ensemble of solutions whose complexity is reflected by the interpreted noise in the data. The data uncertainty determines how accurately the measurements should be fit. Consequently, one should not view Figure 5 in quite the same way as would be done for a linearized inversion because data noise and unmodeled effects are also accounted for. Furthermore, the average model is only one measure of the ensemble of solutions, and it would be possible to select individual models that have smaller rms residuals (e.g., Shapiro et al., 2004; Behr et al., 2010; Moschetti et al., 2010).

Synthetic resolution tests are performed to analyze the resolving power of the data (Figure 6a). Noise with a standard deviation equal to the peak of the corresponding posterior probability distribution of noise for the actual data set is added to the synthetics. The standard deviation of the noise added to the 1-, 4-, 8-, and 12-s data sets is 1.05, 0.44, 0.31, and 0.43 s, respectively. The true model has been designed to demonstrate the capability of the method to retrieve velocity discontinuities, smooth velocity transitions, and structures of varying scales. The maximum perturbation of the alternating rectangles is ±0.3 km/s. The original pattern is best retrieved for periods between 2 and 10 s. For a 1-s period, the pattern is less precisely recovered due to the large estimated data variance, which makes a more detailed image unjustified. Maps of periods >10 s lack sufficient raypath coverage for more detailed resolution. The same resolution test is applied to the data set again, but this time using the more traditional inversion technique of Young et al. (2011) (Figure 6b-6d). Here, phase velocity variations are mapped
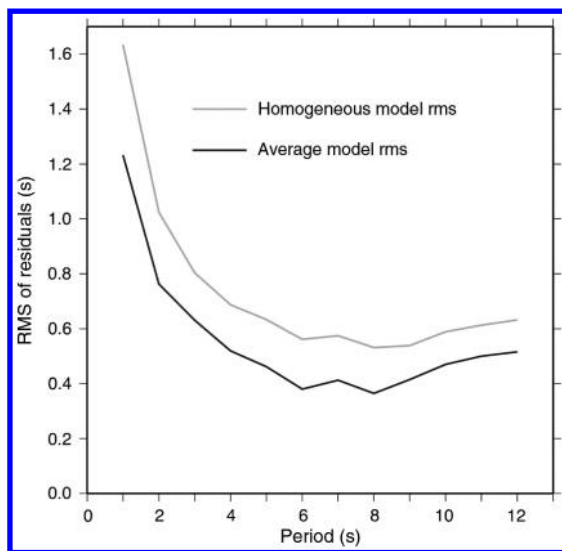

Figure 5. Graph of the rms of the residuals versus period for the transdimensional inversion for phase velocity. The homogeneous model rms values are calculated from a homogeneous model with a velocity equal to the average velocity at that period. The average model rms values are calculated from the final average model of the Bayesian tomographic inversion.

on a regular grid of 3600 nodes using an iterative, nonlinear tomographic inversion scheme, which uses the same eikonal forward solver used by the transdimensional inversion scheme to predict traveltimes and a subspace scheme to solve the inverse problem. Damping and smoothing regularization is applied to manage the trade-off between model roughness and data fit. However, the choice of these parameter values is ad hoc; without more information about the noise content of the data, there is no objective method for determining which solution best describes the data. Models resulting from different combinations of smoothing and damping values are shown in Figure 6b-6d. Again, random noise with the same standard deviations as those used in the Bayesian synthetic test inversion has been added to the synthetic data. However, unlike the Bayesian inversion scheme, which is able to accurately determine the noise in the data, this linear method requires the user to provide an estimate for the standard deviation of the noise. We use the value of 0.25 s for all periods as implemented by Young et al. (2011).

The retrieved map for a 1-s period in Figure 6b reveals an obvious consequence of incorrect noise estimation. The actual standard deviation of the noise (∼1.05 s) is vastly underestimated, resulting in an overly complicated model based primarily on noise when smoothing and damping are not strongly applied. A better result is achieved when damping and smoothing are increased, which is equivalent to assuming a higher level of data noise, as the two trade off against each other. This illustrates the importance of accurate noise estimation. The 12-s maps suffer from elongated streaks, which are a well-known smearing artifact of the inversion method's heavy dependence on raypath configuration; this effect is absent from the Bayesian inversion results. Another advantage of the Bayesian inversion method is that it is much more accurately able to recover the strong velocity discontinuity between the two north–south bars of contrasting velocities. This sharp transition can coexist along with smooth variations because the averaging process over a large number of Voronoi models results in a natural smoothing that is spatially variable and determined by the data, whereas the smoothing imposed in a standard tomographic approach is generally global. This method also provides a more reliable estimate of absolute velocities, whereas in the linear inversion results, absolute velocity is heavily dependent on smoothing and damping.

When applying the linear inversion method to the real data used in this study, we can assume that similar adverse effects will be present (Figure 7). Here the smoothing and damping regularization parameters match those of Young et al. (2011) and are uniformly applied to the data, regardless of raypath coverage or relative data uncertainty. Here, while artifacts due to noise may be subdued, actual details in the model may be indiscriminately lost as well. The heterogeneity seen in the map of the 1-s period data (Figure 7a) is of much shorter wavelength than that of the corresponding Bayesian inversion result. In the latter case, we know that the noise level of the data cannot support much detail. As in the checkerboard test, the 12-s map (Figure 7d) from the linear inversion exhibits elongated, streaky anomalies. For the Bayesian inversion (Figure 4), the result of poorer raypath coverage is decreased detail rather than poorly constrained, elongated anomalies, which are almost certainly an artifact of the raypath configuration. The maps from the two inversion methods for 4 and 8 s are more similar to each other, however.

The most pronounced feature of the phase velocity maps is the low-velocity zone within the neighborhood of the Tamar River

(Figure 1) that continues southward through both arrays. This broad (∼75 km) feature follows a curved path that can be tracked southeast from Tasmania's north coast before bending southward at around 42° S. The anomaly is less pronounced in the south for the shortest periods and then becomes broader at periods greater than 10 s. We also find significantly lower velocities beneath the Dundas Trough to the west. Although not as pronounced as the velocity low along the Tamar River, this narrower (∼40 km) lineation of decreased velocities is manifest at all periods and extends westward and eastward as the period increases. These results are in broad agreement with the previous phase velocity maps for this region produced by Young et al. (2011) using a linear inversion method.

INVERSION OF DISPERSION CURVES

Data

To constrain a 3D shear wave velocity model, we first discretize each phase velocity map into a uniform grid of 13,685 nodes or pixels, which provides a spatial resolution of approximately 3 km. We found that using a finer grid spacing produced the same results, making increased sampling unnecessary. For further analysis, we choose to only use the 2952 data points located within the confines of the seismic array. We sample the phase velocity maps at each node of interest and create a corresponding set of phase velocity curves. The curves are already complete with uncertainty information because we can extract the standard deviation of the
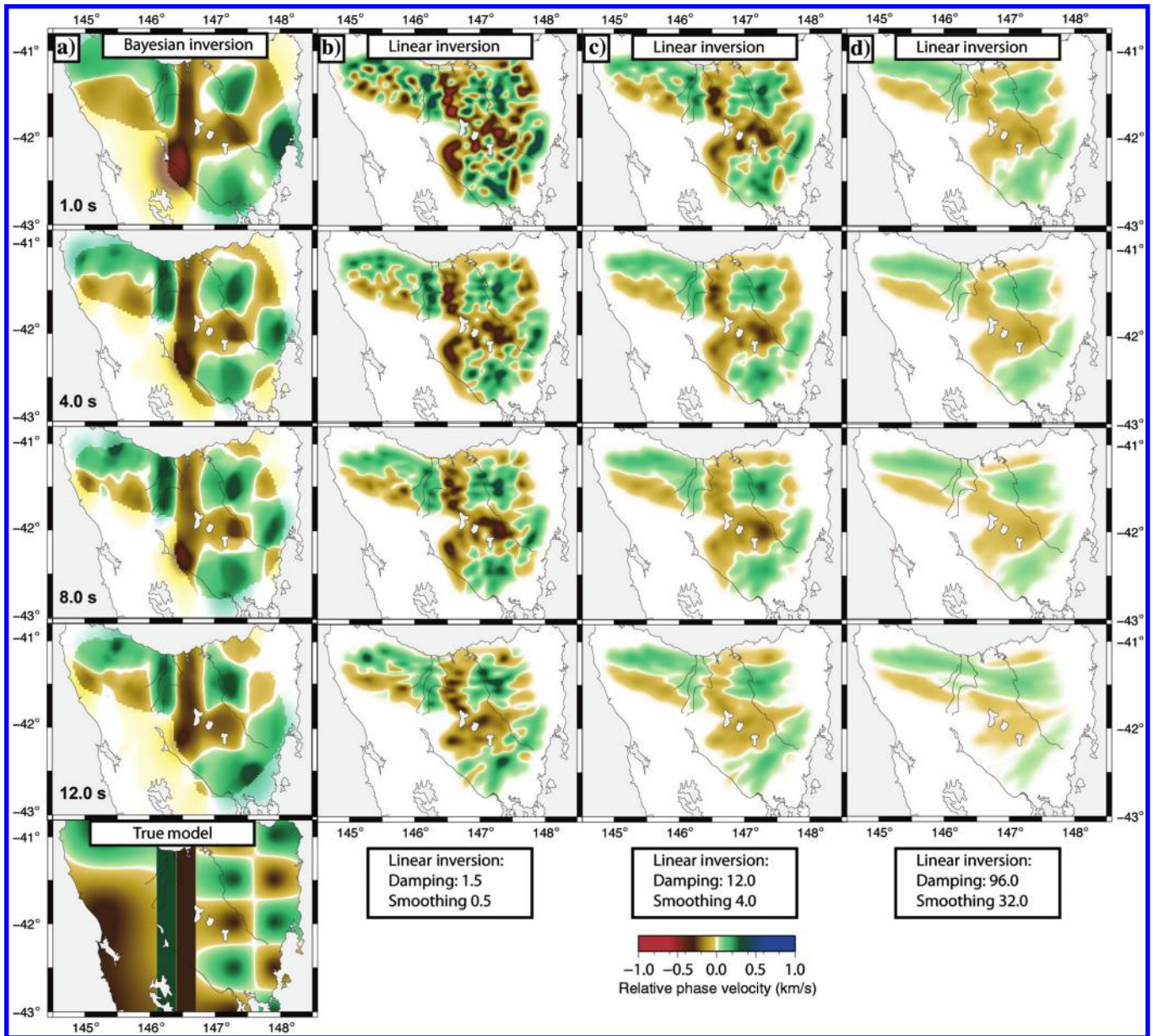

Figure 6. Results of the synthetic resolution test for the Bayesian inversion method (a) and the linearized inversion (b-d). Linear inversion results of applying smoothing and damping parameters of (b) 1.5 and 0.5, (c) 12.0 and 4.0, and (d) 96.0 and 32.0 are shown. The standard deviations of the noise added to all 1-, 4-, 8-, and 12-s data sets are 1.05, 0.44, 0.31, and 0.43 s, respectively. The maximum velocity perturbation of the rectangles is ±0.3 km/s.

posterior probability distribution of the velocity at each pixel of the phase velocity maps. This is a significant step forward, as previous inversion schemes use improvised methods of estimating the spatial distribution of uncertainty of the phase velocity maps prior to the inversion for shear velocity, e.g., Shapiro and Ritzwoller (2002); Bensen et al. (2009). Pixels for which the velocity varies widely throughout the post-burn-in iterations will have a large standard deviation, and thus a larger uncertainty. An explanation of the inversion of the phase velocity curves for 1D shear velocity models, the merging of the resulting shear velocity models, and the creation of a pseudo-3D representation of the shear velocity structure of Tasmania is provided in the following sections.

Inversion method

Each phase velocity curve is inverted for a 1D shear velocity model using the same hierarchical, transdimensional Bayesian technique as before. Bodin et al. (2012b) provide a more detailed description of the surface wave dispersion curve inversion procedure in the context of joint inversion of surface wave group dispersion and receiver functions. The model is described by a variable number of homogeneous horizontal layers, and the number, position, and velocity of the layers are all unknowns in the inverse problem. Similar to the inversion for 2D phase velocity, we also invert for the noise in the data. The forward method used to calculate the phase velocity dispersion is DISPER80, developed by Saito (1988). We assume unobtrusive prior knowledge about the shear velocity model by setting relatively wide bounds of between 2 and 5 km/s for the allowed shear velocity variation during the inversion. Also, we allow between 2 (the minimum allowed by the method) and 30 layers to describe the uppermost 15 km of the crust. Each resulting

shear model is the average of an ensemble of 100,000 model iterations on each of 120 CPU cores (30 CPU hours per 1D inversion).

The data noise parameter retrieved from the inversion is represented by λ. Here the uncertainty of each phase velocity value is assumed to be proportional to the standard deviation associated with that value, with the constant of proportionality λ serving as an unknown in the problem. The standard deviation at a particular period for a particular curve is extracted from the posterior velocity distributions resulting from the previous phase velocity inversion step. The noise of each measurement determines its relative weight in the inversion such that very noisy data (having large standard deviations) do not disproportionately influence the final solution.

Results

We perform a synthetic test to illustrate the benefits of using the standard deviations from the phase velocity maps. An alternative would be to assume all phase velocity values, regardless of period, have the same uncertainty for a given curve. In our synthetic test, we assume a known, simple three-layer model of the upper 15 km of crust. We calculate the corresponding phase velocity curve and randomly add noise of up to ±0.05 km/s to all but one value (associated with the 6-s period). To this remaining value, we add a 0.25 km/s error to mimic the presence of an outlier. The curve is then inverted for a shear velocity model, first assuming that the uncertainty of each velocity value is proportional to the error added to the curve. The results are shown in Figure 8a-8c. The mean of the posterior shear velocity distributions at each depth is in good agreement with the velocities of the actual model. The largest discrepancies arise at velocity discontinuities, to which phase velocity curves are less sensitive. The number of layers (three) is accurately retrieved, as illustrated by the histograms that reflect the posterior probability distribution of the most likely number of layers needed to represent the data (Figure 8c). From the best fitting curve, the solution is only minimally affected by the large outlier velocity value at a 6-s period (Figure 8b). Next, the same curve is inverted assuming equal uncertainty among the phase velocity measurements (Figure 8d-8f). Here, the actual model is slightly less well retrieved (rms misfit of 0.14 km/s versus 0.09 km/s), and the standard deviation of the posterior shear velocity distributions at each depth is larger (0.58 versus 0.50 km/s; Figure 8a). Again, the number of layers is accurately recovered; however, this time with slightly less certainty. The best-fitting curve is significantly more distorted due to the erroneous phase velocity value at 6 s. The inversion is not able to identify this value as being less reliable than the others.

To demonstrate the advantages of using a Bayesian technique over more traditional methods, we use the same test model to perform a synthetic inversion using the non-Bayesian NA of Wathelet (2008). This method requires the user to predetermine, in part, the model parameterization. The number of layers is set to three based on results of the Bayesian inversion. Each horizontal layer is described by a constant velocity. The
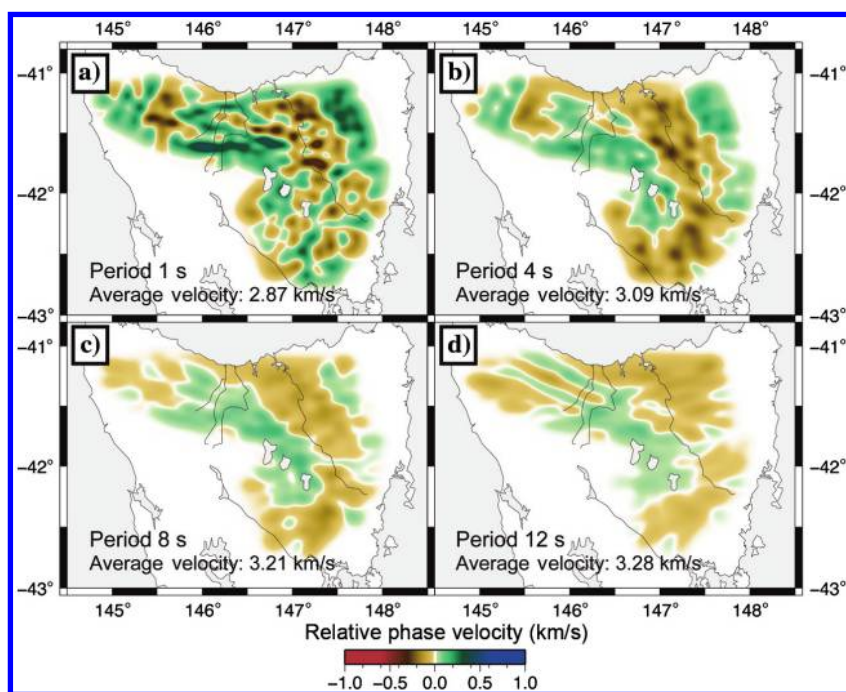

Figure 7. Average phase velocity maps for periods of 1.0, 4.0, 8.0, and 12.0 s as produced from a linearized inversion technique. Phase velocities are plotted relative to the average phase velocity for a given period (noted in the bottom left of each subfigure).

thickness, position, and velocity of each layer are allowed to vary throughout the inversion. Each phase velocity measurement is given equal weight, unlike the Bayesian method, which assigns weights based on the relative noise of each measurement. The same depth (0–15 km) and velocity (2–5 km/s) limits apply. A comparison between the two solutions (Figure 9a, 9b) shows that the NA is less capable of retrieving the true model. Most obviously, the mean of the velocity distribution fails to recover the high-velocity zone between 6- and 10-km depth.

We apply the NA method to two dispersion curves from the actual data set as well (Figure 9d-9i). Although in this case we do not know the actual structure, the resulting average model of the Bayesian inversion contains more detailed features than that of the NA method (Figure 9d, 9g). This is due to the permitted variation in layer number throughout the inversion. Although there are far fewer models with significantly greater than the average number of layers contributing to the final ensemble, these iterations add valuable information about model complexity. The standard deviations of the mean model are also much smaller for the Bayesian inversion, meaning that the most likely model is retrieved with greater certainty. Of notable difference between the Bayesian and NA results for the two real data applications is that the NA method retrieves a very thin low-velocity layer in the uppermost crust (Figure 9e, 9h). This feature is not present in the Bayesian inversion results. The reason for this is likely because the Bayesian method does not permit such a localized low-velocity zone given the noise and number of data.

We have shown that the Bayesian method of surface wave inversion is best at recovering 1D shear velocity profiles from surface wave dispersion data. Because surface wave dispersion is not very sensitive to sharp discontinuities in elastic properties with depth, the degree of vertical smoothing depends on the noise and number of the input data; data of greater number and certainty enable finer vertical resolution of velocity structure. Most of the resulting shear velocity models derived from the Tasmanian data set are

relatively simple and are best described by three to six layers (e.g., Figure 9d, 9g).

Three-dimensional crustal model of Tasmania

At this point in the inversion procedure, we have a discrete, regular sampling of 3D shear velocity space for the uppermost 15 km of the Tasmanian crust. Each point is represented by a shear velocity posterior probability distribution curve rather than a single velocity value. To visualize the results, the average of the posterior probability distribution at a given depth is extracted from each of the 1D shear velocity models. The velocity values are then plotted according to their respective geographic location. In this sense, each shear velocity value extracted from a 1D model represents a single pixel in the image. For purely aesthetic reasons, the resulting grid of velocity pixels is then transformed into a continuous curvature surface using the generic mapping tools package of Wessel and Smith (1995) (Figure 10) to smooth out the pixelation (3-km resolution) of the image. The same procedure can be applied to 2D slices in longitude and latitude as well. The spatial variation of uncertainty can be assessed by viewing a similar surface of standard deviations. For each pixel, the standard deviation of the shear velocity can be extracted from the representative ensemble of shear models for a given depth (Figure 11).

The maximum velocity perturbations of the 1-km depth slice may be subdued as a result of the greater uncertainty in the phase velocity dispersion curves at short periods (Figure 4a, right), which are most sensitive to the uppermost few kilometers of the crust. This elevated error estimate makes strong perturbations in shear velocity unwarranted at this depth. The fact that the permitted amount of variation among the uppermost few kilometers of the shear velocity models is decreased may also be a contributing factor to the relatively low average standard deviation value for the 1-km depth slice (Figure 11a). The average standard deviation increases with depth, likely in response to the decreasing sensitivity of phase velocity to
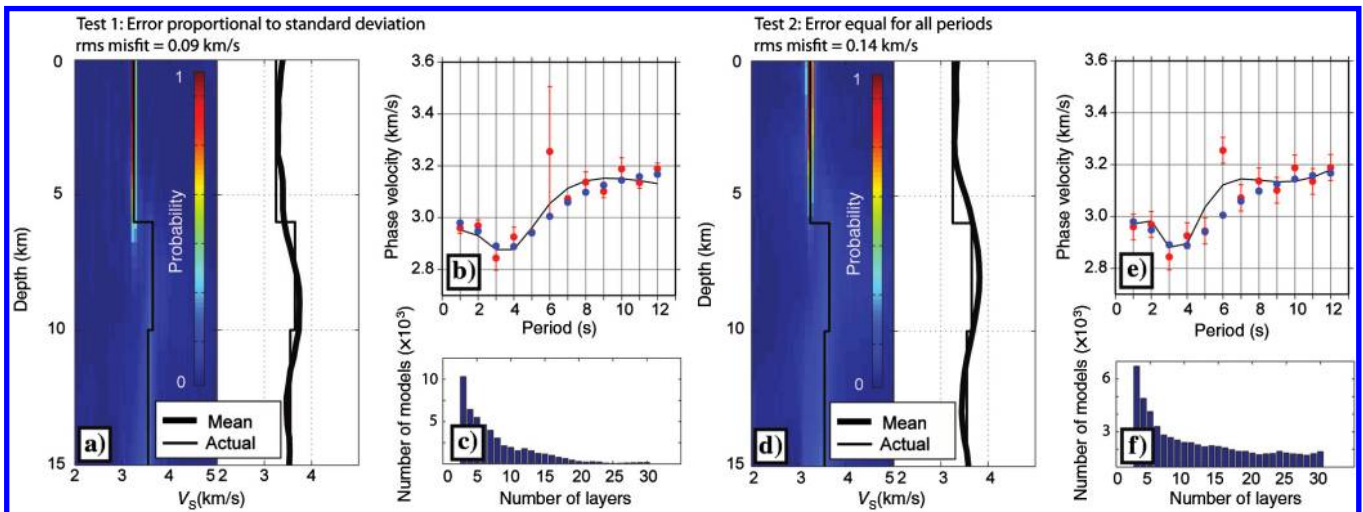

Figure 8. Ensemble solutions for crustal shear velocity from two synthetic tests. Test 1 (a-c) treats the noise in the phase velocity measurements as being proportional to the input standard deviations. Test 2 (d-f) treats the noise as being equal for all periods. To the right of each color density plot is the mean of the velocity distribution at each depth. Also shown are the phase velocity curves associated with the best fitting shear velocity model (black lines) overlaid on the actual phase velocity values of the curve (red dots) (b, e). Standard deviations are shown by red bars, and the original phase curve prior to the addition of random noise is shown by blue dots. (c, f) Histograms representing the accompanying posterior probability distribution functions for the number of layers in the models.

shear velocity as depth increases. At shallow depths, a small change in shear velocity produces a large change in phase velocity, yielding greater certainty in the inversion. On the other hand, decreased sensitivity is manifested by increased uncertainty estimates. For a period of 12 s, phase velocity sensitivity to shear velocity starts to drop off sharply at around a 15-km depth, depending on the earth model (Yang, 2010). For this reason we choose 15 km as the depth limit of our 3D shear velocity model.

Horizontal and vertical slices (Figures 10 and 12) reveal that as in the phase velocity maps, there is a definite and consistent north–south-orientated low-velocity zone, although the low velocities at the shallowest depths in the northern half of the anomaly are in part due to a patch of sediments in the Longford Basin of north Tasmania (Direen and Leaman, 1997), there appears to be a strong change in crustal properties extending to at least a 15-km depth, the limit of our 3D velocity model. The anomaly broadens to the east, whereas the southern extreme becomes less pronounced and more patchy as depth increases.

An east–west slice (Figure 13) taken at a latitude of −41.23° reveals the general east-dipping trend of the low-velocity zone. This feature agrees well with the tectonic model outlined by Reed (2001) and Reed et al. (2002), in which the joining of the ETT and the WTT represents the change from east to west of Paleozoic oceanic to Proterozoic continental basement. In this model, periods of orogeny, sediment deposition, and shortening of up to 90% severely deformed the oceanic crust of the ETT (Reed, 2001). The substantial shortening that took place during the Ordovician and Silurian was likely accommodated by the presence of multiple shear zones with fluid inclusions and elevated temperatures. Recent surface heat flow measurements (Figure 13) reveal a significant thermal anomaly in central eastern Tasmania that is likely due to buried high-heat-producing granite batholiths (KUTh Energy, 2012) emplaced during the Devonian (McClenaghan, 2006) and would contribute to the reduced shear wave speeds seen in our model (Karato, 1993).

The WTT continental crust was spared significant deformation and did not experience the same shortening event. Reed (2001) places the ETT and WTT boundary between the Tamar River and the Port Sorell embayment to the west. This location agrees well with the western edge of the low-velocity zone along the Tamar River. Moreover, the breadth of the anomaly indicates a zone of deformation much wider than the relatively narrow TFS that has been hypothesized to represent the joining of two distinct crustal blocks (Williams, 1989). Our results provide one more piece of evidence that the TFS, which straddles the Tamar River Valley, is merely a thin-skinned feature resulting from a final bout of folding during the Devonian and that ETT and WTT have been passively joined since the Ordovician.

A solid tectonic link between Tasmania and mainland Australia has remained elusive until quite recently, when Direen and Crawford (2003) found paired suites of olivine-rich mafic volcanics and boninites in western Tasmania and the mainland. This discovery added further momentum to the idea that the early Paleozoic Tyennan Orogeny, which shaped western Tasmania, is part of a much larger orogenic cycle that manifested as the Delamerian Orogeny in mainland southeast Australia and the Ross Orogeny in Northern Victoria Land, Antarctica. A connection between eastern Tasmania and the mainland has also been postulated (Talent and Banks, 1967; Powell and Baillie, 1992), with several authors (Foster and Gray, 2000; Reed, 2001; Cayley et al., 2002; Fergusson, 2003) pointing out that the Tabberabbera Zone east of Melbourne experienced Ordovician to Silurian orogenesis and appears to overlie oceanic basement. Reed (2001) therefore suggests that the boundary between WTT and ETT is a southerly continuation of the boundary between the Melbourne Zone and Tabberabbera Zone represented on the mainland by the Governor Fault. In this scenario, Cayley et al. (2002) and Cayley

Figure 9. Ensemble solutions for crustal shear velocity from the Bayesian methods of this study and the NA for a synthetic case (a, b) and two real data examples (d, e, g, h). To the right of each color density plot is the mean of the velocity distribution at each depth. At the bottom are the corresponding phase velocity curves (red dots) and for the synthetic case, the actual curve (blue dots). The amount of noise added to the curves is shown by red error bars.

(2011) see the basement underlying the Melbourne Zone sediments as a northward continuation of Proterozoic western Tasmania, and they invoke the idea of an exotic microcontinent to explain the presence of much older rocks in a region of Victoria characterized by early mid-Paleozoic exposure. Although our results are somewhat equivocal with regard to the existence of a Proterozoic microcontinent, they do point to the presence of highly deformed oceanic crust beneath ETT, which is consistent with the idea that it represents the southern extension of the mainland Tabberabbera Zone. Furthermore, the Governor Fault in Victoria is approximately east dipping (Cayley et al., 2002), which agrees with the dip direction of the low-velocity zone we image in Tasmania.

An anomaly beneath the Tamar River has been observed in other data sets, including conductivity and heat flow patterns (Parkinson et al., 1988; KUTh Energy, 2012), and reflection, refraction, and teleseismic studies (Rawlinson et al., 2010b). The results of this study provide conclusive evidence that the anomaly is deep seated, eastward dipping, and not an artifact of vertical smearing of a shallow feature (e.g., shallow sediments) that teleseismic tomography cannot alone rule out. Our model also provides better and more consistent resolution of the feature than existing reflection and refraction experiments can provide (Rawlinson and Urvoy, 2006). We propose that the low-velocity zone is the result of pronounced deformation associated with the shortening, thickening, and accretion of oceanic crust along the passive margin of Tasmania during the early mid-Paleozoic, coupled with intrusion of heat-producing granites in the Devonian. In this case, we would expect the seismic velocity signature to be wide and deep as seen in our 3D model.

Another prominent element of the shear velocity model is the low-velocity anomaly beneath the northwest corner of Tasmania (Figure 13). The western edge closely follows the Arthur Lineament, a sheared belt of magnetic metamorphic rocks that separates the Rocky Cape Block from the Dundas Trough (Seymour et al., 2007). This anomaly dips to the east (Figure 13) and supports the interpretation that Tasmania was initially drawn into an east-dipping subduction zone in the Middle Cambrian before being obducted westward into an arc-continent collision (Crawford et al., 2003; Gibson et al., 2010; Cayley, 2011).

The strength and eastward trend with depth of the anomaly could therefore be interpreted as the vestige of the initial eastward-dipping phase of subduction during the mid-Cambrian Tyennan Orogeny. The low-velocity zone in our model beneath the Dundas Trough is consistent with a
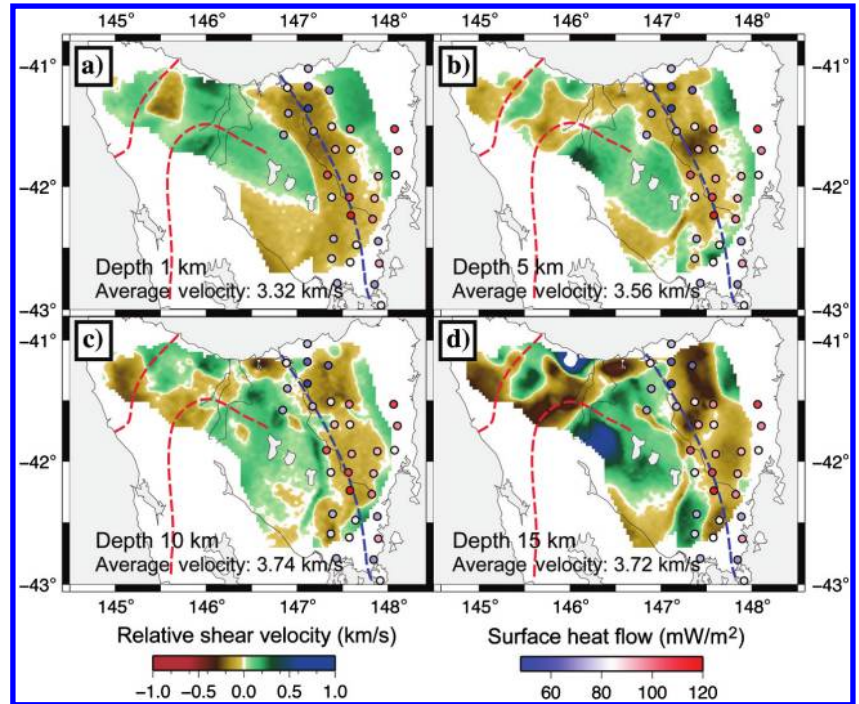

Figure 10. Horizontal slices taken at a series of depth intervals through the 3D shear velocity model. Velocity perturbations are shown with respect to the average shear velocity at the given depth, which is noted beneath each 2D slice. The dashed red lines indicate the boundary of the Dundas Trough, whereas the dashed blue lines indicate the approximate location of the TFS. Recent surface heat flow measurements from KUTh Energy (2012) are shown by color-coded circles.
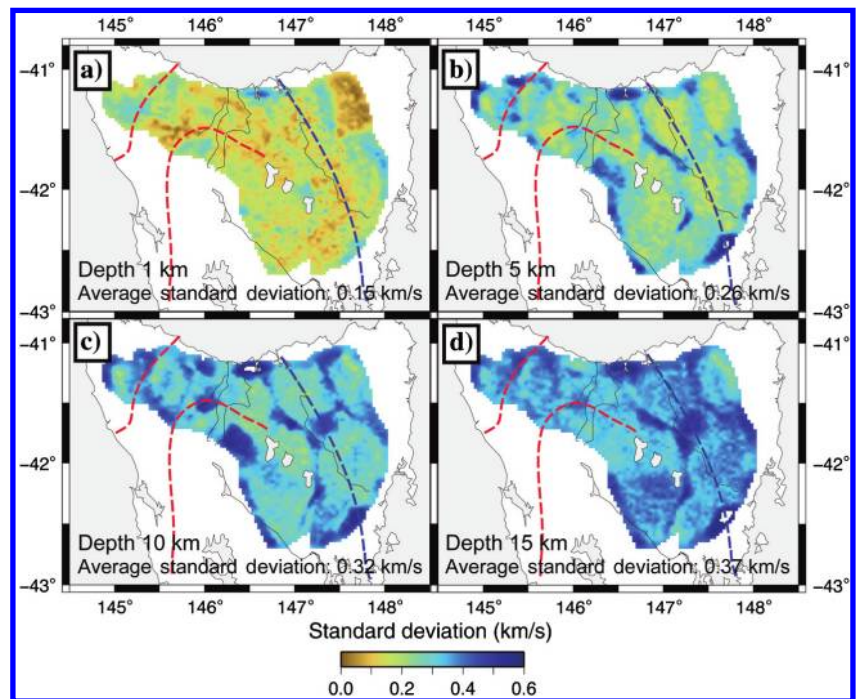

Figure 11. Horizontal slices taken at a series of depth intervals through the standard deviations of the 3D shear velocity model shown in Figure 10. The dashed lines are as in Figure 10.

transition that is heavily deformed and composed of mainly sedimentary rock, and because, like the Tyennan Orogeny, the coeval Delamerian Orogeny of mainland southeast Australia experienced eastward dipping subduction, it generates further evidence in support of the direct connection between Tasmania and the neighboring mainland.

The elongated high-velocity zone identified in Figure 13 in the uppermost ∼3 km of the crust between the two low-velocity anomalies may be a signature of extensive dolerite sheets emplaced during the Jurassic (Brauns et al., 2000). A similar shallow area of elevated velocity to the east is attributable to the Devonian granites of ETT (Patison et al., 2001). The high resolution potential of our method justifies analysis of model features on the horizontal scale of ∼10 km. For example, the high-velocity anomaly along the north

edge of the TIGGER array at about 146° longitude (Figure 10) underlies the Forth metamorphic complex (Figure 1), which was formed and exhumed during the Cambrian Delamerian Orogeny and contains Proterozoic quartzite, amphiolite, phyllite, and schist (Meffre et al., 2000). Interestingly, the Badger Head metamorphic complex (Figure 1), which lies about 75 km west of the Forth metamorphic complex, overlies a localized low-velocity zone. The Proterozoic sedimentary rocks of this structurally complex turbidite package are intensely deformed, highly metamorphosed, and they are considered allochthonous (Leaman et al., 1973; Reed et al., 2002). Metamorphic grade for the complex is mostly lower greenschist facies (Reed et al., 2002), whereas the Forth metamorphic complex experienced higher temperatures and pressures with metamorphism ranging from upper greenschist to upper amphibolite facies (Foster et al., 2005). The difference in shear velocity beneath these two complexes likely arises from compositional and density differences.

CONCLUSIONS

We presented a scheme for producing a 3D shear velocity model from ambient seismic noise dispersion measurements using fully nonlinear Bayesian techniques. Model parameters, such as the number of layers, data variance, and model complexity, are left as unknowns in the inversion and are therefore driven by the information content of the data. Using a transdimensional approach, we first calculate 2D phase velocity maps for a range of periods. From these maps, 1D dispersion curves, complete with standard deviations, are produced at a regular grid of points in latitude and longitude. Each curve is independently inverted for a 1D shear velocity model. The 1D models are then joined together to create a pseudo-3D map of the shear velocity structure. Unlike more conventional methods that often use ad hoc error estimation, we preserve uncertainty information from each step and use it to further constrain the next step in the inversion. Each inversion, whether for 2D phase velocity variations or a 1D shear velocity model, is uniquely parameterized according to the quantity, quality, and distribution of the input data.

We apply our method to data from two adjacent, densely spaced seismic arrays in Tasmania. Phase velocity maps for periods between 1 and 12 s and a 3D shear velocity model down to a depth of 15 km are produced. The resulting tomographic images reveal a ∼75 km-wide, southeast-trending, eastward-dipping, velocity lineation within the vicinity of the Tamar River. This feature is likely the result of strong deformation and faulting associated with the Phanerozoic accretion of oceanic material along the more rigid Proterozoic continental Tasmanian lithosphere. To the west, a pronounced low-velocity zone is also present beneath the Dundas Trough of northwest Tasmania. The eastward-dipping geometry of this anomaly suggests an association with the deformation and shortening of the Tyennan Orogeny and supports a connection between Tasmania and mainland Australia since the Cambrian.
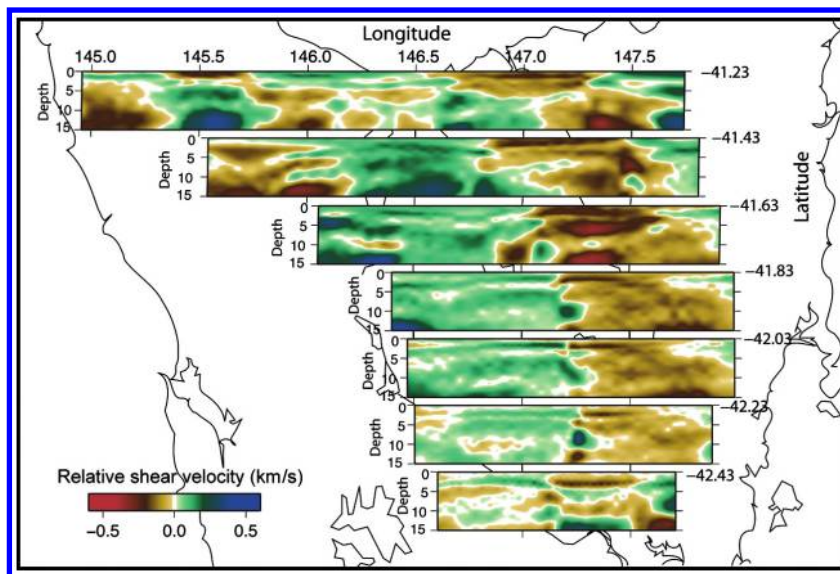

Figure 12. Vertical slices taken at regular intervals in latitude through the 3D shear velocity model. Velocity perturbations are shown with respect to the average shear velocity with depth, which is calculated at 0.5-km intervals. The depth axis has been stretched by 100% to facilitate easier viewing of the depth dependence of the perturbations. The location of the transect of each depth section is denoted by its zero depth line.
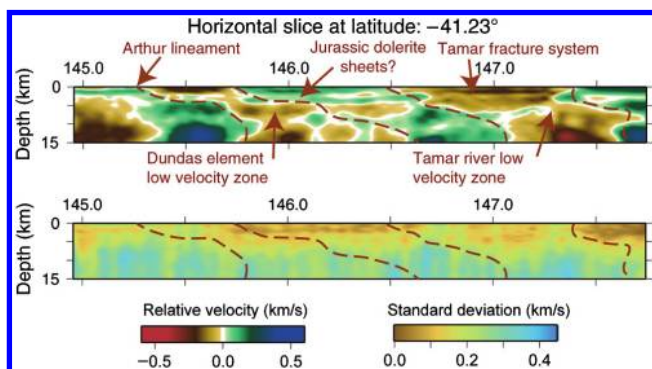

Figure 13. Vertical shear velocity and standard deviation slices taken at −41.23° latitude. Features and velocity anomalies mentioned in the text are highlighted.

REFERENCES

Arnold, R., and J. Townend, 2007, A Bayesian approach to estimating tectonic stress from seismological data: Geophysical Journal International, **170**, 1336–1356, doi: 10.1111/j.1365-246X.2007.03485.x.

Bayes, T., 1763, An essay towards solving a problem in the doctrine of chances: Philosophical Transactions of the Royal Society of London, **53**, 370–418, doi: 10.1098/rstl.1763.0053.

Behr, Y., J. Townend, S. Bannister, and M. Savage, 2010, Shear velocity structure of the Northland Peninsula, New Zealand, inferred from ambient noise correlations: Journal of Geophysical Research, **115**, B05309, doi: 10.1029/2009JB006737.

Behr, Y., J. Townend, S. Bannister, and M. K. Savage, 2011, Crustal shear wave tomography of the Taupo Volcanic Zone, New Zealand, via ambient noise correlation between multiple three-component networks: Geochemistry, Geophysics, Geosystems, **12**, Q03015, doi: 10.1029/2010GC003385.

Bensen, G., M. Ritzwoller, and Y. Yang, 2009, A 3-D shear velocity model of the crust and uppermost mantle beneath the United States from ambient seismic noise: Geophysical Journal International, **177**, 1177–1196, doi: 10.1111/j.1365-246X.2009.04125.x.

Bensen, G. D., M. H. Ritzwoller, M. P. Barmin, A. L. Levshin, F. Lin, M. P. Moschetti, N. M. Shapiro, and Y. Yang, 2007, Processing seismic ambient noise data to obtain reliable broad-band surface wave dispersion measurements: Geophysical Journal International, **169**, 1239–1260, doi: 10.1111/j.1365-246X.2007.03374.x.

Bensen, G. D., M. H. Ritzwoller, and N. M. Shapiro, 2008, Broadband ambient noise surface wave tomography across the United States: Journal of Geophysical Research, **113**, B05306, doi: 10.1029/2007JB005248.

Bernando, J., and A. Smith, 1994, Bayesian theory: John Wiley & Sons, Ltd.

Berry, R. F., D. A. Steele, and S. Meffre, 2008, Proterozoic metamorphism in Tasmania: Implications for tectonic reconstructions: Precambrian Research, **166**, 387–396, doi: 10.1016/j.precamres.2007.05.004.

Bodin, T., and M. Sambridge, 2009, Seismic tomography with the reversible jump algorithm: Geophysical Journal International, **178**, 1411–1436, doi: 10.1111/j.1365-246X.2009.04226.x.

Bodin, T., M. Sambridge, N. Rawlinson, and P. Arroucau, 2012a, Transdimensional tomography with unknown data noise: Geophysical Journal International, **189**, 1536–1556, doi: 10.1111/j.1365-246X.2012.05414.x.

Bodin, T., M. Sambridge, H. Tkalčić, P. Arroucau, K. Gallagher, and N. Rawlinson, 2012b, Transdimensional inversion of receiver functions and surface wave dispersion: Journal of Geophysical Research, doi: 10.1029/2011JB008560.

Box, G., and G. Tiao, 1973, Bayesian inference in statistical analysis: John Wiley & Sons, Inc.

Brauns, C. M., J. M. Hergt, J. D. Woodhead, and R. Maas, 2000, Os isotopes and the origin of the Tasmanian dolerites: Journal of Petrology, **41**, 905–918, doi: 10.1093/petrology/41.7.905.

Cayley, R., 2011, Exotic crustal block accretion to the eastern Gondwanaland margin in the Late Cambrian — Tasmania, the Selwyn Block, and implications for the Cambrian-Silurian evolution of the Ross, Delamerian, and Lachlan orogens: Gondwana Research, **19**, 628–649, doi: 10.1016/j.gr.2010.11.013.

Cayley, R. A., D. H. Taylor, A. H. M. VandenBerg, and D. H. Moore, 2002, Proterozoic — Early Palaeozoic rocks and the Tyennan Orogeny in central Victoria: The Selwyn Block and its tectonic implications: Australian Journal of Earth Sciences, **49**, 225–254, doi: 10.1046/j.1440-0952.2002.00921.x.

Clitheroe, G., O. Gudmundsson, and B. Kennett, 2001, Sedimentary and upper crustal structure of Australia from receiver functions: Australian Journal of Earth Sciences, **47**, 209–216, doi: 10.1046/j.1440-0952.2000.00774.x.

Crawford, A. J., S. Meffre, and P. A. Symonds, 2003, 120 to 0 Ma tectonic evolution of the southwest Pacific and analogous geological evolution of the 600 to 220 Ma Tasman Fold Belt System, in R. R. Hillis, and R. D. Muller, eds., The evolution and dynamics of the Australian plate: Geological Society of America, Special Publications, 25–40.

Direen, N. G., and A. J. Crawford, 2003, Fossil seaward-dipping reflector sequences preserved in southeastern Australia: A 600 Ma volcanic passive margin in eastern Gondwanaland: Journal of the Geological Society, **160**, 985–990, doi: 10.1144/0016-764903-010.

Direen, N. G., and D. E. Leaman, 1997, Geophysical modelling of structure and tectonostratigraphic history of the Longford Basin, northern Tasmania: Exploration Geophysics, **28**, 29–33, doi: 10.1071/EG997029.

Dorman, J., and M. Ewing, 1962, Numerical inversion of seismic surface wave dispersion data and crust-mantle structure in the New York-Pennsylvania area: Journal of Geophysical Research, **67**, 5227–5241, doi: 10.1029/JZ067i013p05227.

Eberhart-Phillips, D., and M. Reyners, 1999, Plate interface properties in the northeast Hikurangi subduction zone, New Zealand, from converted seismic waves: Geophysical Research Letters, **26**, 2565–2568, doi: 10.1029/1999GL900567.

Fergusson, C. L., 2003, Ordovician-Silurian accretion of the Lachlan Fold Belt, southeastern Australia: Australian Journal of Earth Sciences, **50**, 475–490, doi: 10.1046/j.1440-0952.2003.01013.x.

Foster, D. A., and D. R. Gray, 2000, Evolution and structure of the Lachlan Fold Belt (Orogen) of eastern Australia: Annual Review of Earth and Planetary Sciences, **28**, 47–80, doi: 10.1146/annurev.earth.28.1.47.

Foster, D. A., D. R. Gray, and C. Spaggiari, 2005, Timing of subduction and exhumation along the Cambrian East Gondwana margin, and the formation of Paleozoic backarc basins: Bulletin of the Seismological Society of America, **117**, 105–116, doi: 10.1130/B25481.1.

Gibson, G., M. Morse, T. Ireland, and G. Nayak, 2010, Arc-continent collision and orogenesis in western Tasmanides: Insights from reactivated basement structures and formation of an ocean-continent transform boundary off western Tasmania: Gondwana Research, **19**, 608–627, doi: 10.1016/j.gr.2010.11.020.

Green, P., 1995, Reversible jump Markov chain Monte Carlo computation and Bayesian model determination: Biometrika, **82**, 711–732, doi: 10.1093/biomet/82.4.711.

Green, P. G., 2003, Transdimensional MCMC, in P. G. Green, N. L. Hjort, and S. Richardson, eds., Highly structured stochastic systems: Oxford University Press, Oxford Statistical Sciences Series, 179–196.

Karato, S., 1993, Importance of anelasticity in the interpretation of seismic tomography: Geophysical Research Letters, **20**, 1623–1626, doi: 10.1029/93GL01767.

Khan, A., A. Zunino, and F. Deschamps, 2011, The thermo-chemical and physical structure beneath the North American Continent from Bayesian inversion of surface-wave phase velocities: Journal of Geophysical Research, **116**, B09304, doi: 10.1029/2011JB008380.

Kissling, E., 1988, Geotomography with local earthquake data: Reviews of Geophysics, **26**, 659–698, doi: 10.1029/RG026i004p00659.

KUTh Energy, 2012, www.kuthenergy.com, accessed 20 July 2012.

Langston, C., 1979, Structure under Mount Rainier, Washington, inferred from teleseismic body waves: Journal of Geophysical Research, **84**, 4749–4762, doi: 10.1029/JB084iB09p04749.

Leaman, D. E., 1994, The Tamar fracture system in Tasmania: Does it exist? Australian Journal of Earth Sciences, **41**, 73–74, doi: 10.1080/08120099408728116.

Leaman, D. E., P. A. Symonds, and J. E. Shirley, 1973, Gravity survey of the Tamar region, northern Tasmania: Geological Survey of Tasmania, Paper 1.

Lin, F., M. Ritzwoller, J. Townend, S. Bannister, and M. Savage, 2007, Ambient noise Rayleigh wave tomography of New Zealand: Geophysical Journal International, **170**, 649–666, doi: 10.1111/j.1365-246X.2007.03414.x.

McClenaghan, M. P., 2006, The geochemistry of Tasmanian Devonian-Carboniferous granites and implications for the composition of their source rocks: Mineral Resources Tasmania Record, 2006-06.

Meffre, S., R. F. Berry, and M. Hall, 2000, Cambrian metamorphic complexes in Tasmania: Tectonic implications: Australian Journal of Earth Sciences, **47**, 971–985, doi: 10.1046%2fj.1440-0952.2000.00825.x.

Mitra, S., S. Kainkaryam, A. Padhi, S. Rai, and S. Bhattacharya, 2011, The Himalayan foreland basin crust and upper mantle: Physics of the Earth and Planetary Interiors, **184**, 34–40, doi: 10.1016/j.pepi.2010.10.009.

Monelli, D., and P. M. Mai, 2008, Bayesian inference of kinematic earthquake rupture paramters through fitting of strong motion data: Geophysical Journal International, **173**, 220–232, doi: 10.1111/j.1365-246X.2008.03733.x.

Moschetti, M. P., M. H. Ritzwoller, F.-C. Lin, and Y. Yang, 2010, Crustal shear wave velocity structure of the western United States inferred from ambient seismic noise and earthquake data: Journal of Geophysical Research, **115**, B10306, doi: 10.1029/2010JB007448.

Myers, S. C., G. Johannesson, and W. Hanley, 2007, A Bayesian hierarchical method for multiple-event seismic location: Geophysical Journal International, **171**, 1049–1063, doi: 10.1111/j.1365-246X.2007.03555.x.

Parkinson, W., R. Hermanto, J. Sayers, N. Bindoff, H. Dosso, and W. Nienaber, 1988, The Tamar conductivity anomaly: Physics of the Earth and Planetary Interiors, **52**, 8–22, doi: 10.1016/0031-9201(88)90053-2.

Patison, N. L., R. F. Berry, G. J. Davidson, B. P. Taylor, R. S. Bottrill, B. Manzi, J. Ryba, and R. E. Shepherd, 2001, Regional metamorphism of the Mathina Group, northeast Tasmania: Australian Journal of Earth Sciences, **48**, 281–292, doi: 10.1046/j.1440-0952.2001.00862.x.

Piana Agostinetti, N., and A. Malinverno, 2010, Receiver function inversion by trans-dimensional Monte Carlo sampling: Geophysical Journal International, **181**, 858–872, doi: 10.1111/j.1365-246X.2010.04530.x.

Powell, C. M., and P. W. Baillie, 1992, Tectonic affinity of the Mathinna Group in the Lachlan Fold Belt: Tectonophysics, **214**, 193–209, doi: 10.1016/0040-1951(92)90197-E.

Rawlinson, N., B. L. N. Kennett, E. Vanacore, R. A. Glen, and S. Fishwick, 2011, The structure of the upper mantle beneath the Delamerian and Lachlan orogens from simultaneous inversion of multiple teleseismic datasets: Gondwana Research, **19**, 788–799, doi: 10.1016/j.gr.2010.11.001.

Rawlinson, N., S. Pozgay, and S. Fishwick, 2010a, Seismic tomography: A window into deep Earth: Physics of the Earth and Planetary Interiors, **178**, 101–135, doi: 10.1016/j.pepi.2009.10.002.

Rawlinson, N., and M. Sambridge, 2004, Wavefront evolution in strongly heterogeneous layered media using the fast marching method: Geophysical Journal International, **156**, 631–647, doi: 10.1111/j.1365-246X.2004.02153.x.

Rawlinson, N., H. Tkalčić, and A. M. Reading, 2010b, Structure of the Tasmanian lithosphere from 3D seismic tomography: Australian Journal of Earth Sciences, **57**, 381–394, doi: 10.1080/08120099.2010.481325.

Rawlinson, N., and M. Urvoy, 2006, Simultaneous inversion of active and passive source datasets for 3-D seismic structure with application to Tasmania: Geophysical Research Letters, **33**, L24313, doi: 10.1029/2006GL028105.

Reed, A. R., 2001, Pre-Tabberabberan deformation in eastern Tasmania: A southern extension of the Benambran Orogeny: Australian Journal of Earth Sciences, **48**, 785–7964, doi: 10.1046/j.1440-0952.2001.00900.x.

Reed, A. R., C. Calver, and R. S. Bottrill, 2002, Palaeozoic suturing of eastern and western Tasmania in the west Tamar region: Implications for the tectonic evolution of southeast Tasmania: Australian Journal of Earth Sciences, **49**, 809–830, doi: 10.1046/j.1440-0952.2002.00955.x.

Saito, M., 1988, DISPER80: A subroutine package for the calculation of seismic normal mode solutions, in D. J. Doornbos, ed., Seismological algorithms: Computational methods and computer programs: Academic Press, 293–319.

Sambridge, M., 1999, Geophysical inversion with a neighbourhood algorithm I. Searching a parameter space: Geophysical Journal International, **138**, 479–494, doi: 10.1046/j.1365-246X.1999.00876.x.

Scales, J., and R. Snieder, 1998, What is noise? Geophysics, **63**, 1122–1124, doi: 10.1190/1.1444411.

Seats, K. J., J. F. Lawrence, and G. A. Prieto, 2012, Improved ambient noise correlation functions using Welch's method: Geophysical Journal International, **188**, 513–523, doi: 10.1111/j.1365-246X.2011.05263.x.

Seymour, D. B., G. R. Green, and C. R. Calver, 2007, The geology and mineral deposits of Tasmania: A summary: Geological Survey Bulletin of Tasmania, 72

Shapiro, N. M., M. Campillo, L. Stehly, and M. H. Ritzwoller, 2005, High-resolution surface-wave tomography from ambient seismic noise: Science, **307**, 1615–1618, doi: 10.1126/science.1108339.

Shapiro, N. M., and M. H. Ritzwoller, 2002, Monte-Carlo inversion for a global shear-velocity model of the crust and upper mantle: Geophysical Journal International, **151**, 88–105, doi: 10.1046/j.1365-246X.2002.01742.x.

Shapiro, N. M., M. H. Ritzwoller, J. C. Mareschal, and C. Jaupart, 2004, Lithospheric structure of the Canadian Shield inferred from inversion of surface-wave dispersion with thermodynamic a priori constraints, in A. Curtis, and R. Wood, eds., Geological prior information: Informing science and engineering: Geological Society of London, Special Publications, 175–194.

Stehly, L., B. Fry, M. Campillo, N. M. Shapiro, J. Guilbert, L. Boschi, and D. Giardini, 2009, Tomography of the Alpine region from observations of seismic ambient noise: Geophysical Journal International, **178**, 338–350, doi: 10.1111/j.1365-246X.2009.04132.x.

Talent, J. A., and M. R. Banks, 1967, Devonian of Victoria and Tasmania, in D. H. Oswald, ed., International symposium on the Devonian system: Alberta Society of Petroleum Geologists, 1, 147–163.

Thurber, C. H., 1992, Hypocenter-velocity structure coupling in local earthquake tomography: Physics of the Earth and Planetary Interiors, **75**, 55–62, doi: 10.1016/0031-9201(92)90117-E.

Villaseñor, A., M. Ritzwoller, A. Levshin, M. Barmin, E. Engdahl, W. Spakman, and J. Trampert, 2001, Shear velocity structure of central Europe from inversion of surface wave velocities: Physics of the Earth and Planetary Interiors, **123**, 169–184, doi: 10.1016/S0031-9201(00)00208-9.

Walck, M. C., and R. W. Clayton, 1987, P wave velocity variations in the Coso Region, California, derived from local earthquake travel times: Journal of Geophysical Research, **92**, 393–405, doi: 10.1029/JB092iB01p00393.

Walsh, D., R. Arnold, and J. Townend, 2009, A Bayesian approach to determining and parameterizing earthquake focal mechanisms: Geophysical Journal International, **176**, 235–255, doi: 10.1111/j.1365-246X.2008.03979.x.

Wang, C., W. Chan, and W. Mooney, 2003, Three-dimensional velocity structure of crust and upper mantle in southwestern China and its tectonic implications: Journal of Geophysical Research, **108**, 2442, doi: 10.1029/2002JB001973.

Wathelet, M., 2008, An improved neighborhood algorithm: Parameter conditions and dynamic scaling: Geophysical Research Letters, **35**, L09301, doi: 10.1029/2008GL033256.

Weaver, R., C. Hadziioannou, E. Larose, and M. Campillo, 2011, On the precision of noise correlation interferometry: Geophysical Journal International, **185**, 1384–1392, doi: 10.1111/j.1365-246X.2011.05015.x.

Wessel, P., and W. Smith, 1995, New version of the generic mapping tools released: EOS — Transactions of the American Geophysical Union, **76**, 329, doi: 10.1029/95EO00198.

Williams, E., 1989, Summary and synthesis, in C. F. Burrett, and E. L. Martin, eds., Geology and mineral resources of Tasmania: Geological Society of Australia, Special Publications, 468–499.

Xu, L., S. Rondenay, and R. D. Van der Hilst, 2007, Structure of the crust beneath the southeastern Tibetan Plateau from teleseismic receiver functions: Physics of the Earth and Planetary Interiors, **165**, 176–193, doi: 10.1016/j.pepi.2007.09.002.

Yang, Y., A. Li, and M. H. Ritzwoller, 2008a, Crustal and uppermost mantle structure in southern Africa revealed from ambient noise and teleseismic tomography: Geophysical Journal International, **174**, 235–248, doi: 10.1111/j.1365-246X.2008.03779.x.

Yang, Y., M. Ritzwoller, A. Levshin, and N. Shapiro, 2007, Ambient noise Rayleigh wave tomography across Europe: Geophysical Journal International, **168**, 259–274, doi: 10.1111/j.1365-246X.2006.03203.x.

Yang, Y., M. H. Ritzwoller, F. C. Lin, M. P. Moschetti, and N. M. Shapiro, 2008b, Structure of the crust and uppermost mantle beneath the western United States revealed by ambient noise and earthquake tomography: Journal of Geophysical Research, **113**, B12310, doi: 10.1029/2008JD009945.

Yang, Y., Y. Zheng, J. Chen, S. Zhou, S. Celyan, E. Sandvol, F. Tilmann, K. Priestley, T. M. Hearn, J. F. Ni, L. D. Brown, and M. H. Ritzwoller, 2010, Rayleigh wave phase velocity maps of Tibet and the surrounding regions from ambient seismic noise tomography: Geochemistry, Geophysics, Geosystems, **11**, Q08010, doi: 10.1029/2010GC003119.

Yao, H., C. Beghein, and R. D. Van der Hilst, 2008, Surface wave array tomography in SE Tibet from ambient seismic noise and two-station analysis — II. Crustal and upper-mantle structure: Geophysical Journal International, **173**, 205–219, doi: 10.1111/j.1365-246X.2007.03696.x.

Yao, H., and R. D. Van der Hilst, 2009, Analysis of ambient noise energy distribution and phase velocity bias in ambient noise tomography, with application to SE Tibet: Geophysical Journal International, **179**, 1113–1132, doi: 10.1111/j.1365-246X.2009.04329.x.

Yao, H., R. D. Van der Hilst, and M. V. de Hoop, 2006, Surface-wave array tomography in SE Tibet from ambient seismic noise and two-station analysis — I. Phase velocity maps: Geophysical Journal International, **166**, 732–744, doi: 10.1111/j.1365-246X.2006.03028.x.

Yolsal-Çevikbilen, S., C. Biryol, S. Beck, G. Zandt, T. Taymaz, H. Adiyaman, and A. Ozacar, 2012, 3-D crustal structure along the North Anatolian Fault Zone in north-central Anatolia revealed by local earthquake tomography: Geophysical Journal International, **188**, 819–849, doi: 10.1111/j.1365-246X.2011.05313.x.

Young, M., N. Rawlinson, P. Arroucau, A. Reading, and H. Tkalčić, 2011, High-frequency ambient noise tomography of southeast Australia: New constraints on Tasmania's tectonic past: Geophysical Research Letters, **38**, L13313, doi: 10.1029/2011GL047971.

Zollo, A., L. D'Auria, R. D. Matteis, A. Herrero, H. Virieux, and P. Gasparini, 2002, Bayesian estimation of 2-D P-velocity models from active seismic arrival time data: Imaging of the shallow structure of Mt. Vesuvius (Southerm Italy): Geophysical Journal International, **151**, 566–582, doi: 10.1046/j.1365-246X.2002.01795.x.